Received: 16 March 2020 | Revised: 24 September 2020 | Accepted: 26 October 2020

DOI: 10.1111/micc.12668

Microcirculation WILEY

ORIGINAL ARTICLE

Effect of cytosol viscosity on the flow behavior of red blood cell suspensions in microvessels

Wei Chien | **Gerhard Gompper** | **Dmitry A. Fedosov**

Theoretical Physics of Living Matter, Institute of Biological Information Processing and Institute for Advanced Simulation, Forschungszentrum Jülich, Jülich, Germany

Correspondence
Dmitry A. Fedosov, Theoretical Physics of Living Matter, Institute of Biological Information Processing and Institute for Advanced Simulation, Forschungszentrum Jülich, 52425 Jülich, Germany.
Email: d.fedosov@fz-juelich.de

FUNDING INFORMATION
This paper was not supported by any source and represents an original effort of the authors.

Abstract

Objective: The flow behavior of blood is strongly affected by red blood cell (RBC) properties, such as the viscosity ratio C between cytosol and suspending medium, which can significantly be altered in several pathologies (e.g. sickle-cell disease, malaria). The main objective of this study is to understand the effect of C on macroscopic blood flow properties such as flow resistance in microvessels, and to link it to the deformation and dynamics of single RBCs.

Methods: We employ mesoscopic hydrodynamic simulations to investigate flow properties of RBC suspensions with different cytosol viscosities for various flow conditions in cylindrical microchannels.

Results: Starting from a dispersed cell configuration which approximates RBC dispersion at vessel bifurcations in the microvasculature, we find that the flow convergence and development of RBC-free layer (RBC-FL) depend only weakly on C, and require a convergence length in the range of $25D$–$50D$, where D is channel diameter. In vessels with $D \leq 20\ \mu m$, the final resistance of developed flow is nearly the same for $C = 5$ and $C = 1$, while for $D = 40\ \mu m$, the flow resistance for $C = 5$ is about 10% larger than for $C = 1$. The similarities and differences in flow resistance can be explained by viscosity-dependent RBC-FL thicknesses, which are associated with the viscosity-dependent dynamics of single RBCs.

Conclusions: The weak effect on the flow resistance and RBC-FL explains why RBCs can contain a high concentration of hemoglobin for efficient oxygen delivery, without a pronounced increase in the flow resistance. Furthermore, our results suggest that significant alterations in microvascular flow in various pathologies are likely not due to mere changes in cytosolic viscosity.

KEYWORDS
cell free layer, cell migration and deformation, flow resistance, smoothed dissipative particle dynamics, viscosity ratio

Abbreviations: BC, boundary condition; COM, center of mass; RBC, red blood cell; RBC-FL, RBC-free layer; SDPD, smoothed dissipative particle dynamics; WCA, Weeks-Chandler-Anderson.

1 | INTRODUCTION

Blood is a multi-component suspension which consists of plasma (≈55%) and cells (red blood cells [RBCs] ≈ 45%, white blood cells and platelets <1%). Flow properties of blood are mainly governed by RBCs,[1-4] which play an important role in many physiological processes. For instance, RBCs are responsible for oxygen delivery and mediate margination (or migration) of platelets[5-7] and leukocytes[8-10] toward vessel walls, thus affecting the hemostatic process and immune response. Blood flow properties are also crucial in many applications, such as the enrichment or separation of rare circulating tumor cells from blood[11,12] and the effectiveness of drug carriers for delivery to the targeted sites.[13-15]

Suspensions of blood cells reveal complex flow properties[4,16] and rheology.[17,18] Two representative examples of the flow behavior of RBC suspension in microvessels or glass capillaries are the Fahraeus[19] and Fahraeus–Lindqvist[20,21] effects. The former effect concerns RBC volumetric flux (or the so-called discharge hematocrit H_d), which appears to be larger than the tube (bulk) hematocrit H_t in vessels with a diameter D in the range of 7–200 μm. The latter effect describes a minimum of blood flow resistance in a tube with a diameter ≈8 μm, such that the resistance to flow increases for both smaller and larger vessel diameters. The main mechanism governing these phenomena is the formation of a RBC depleted region next to the wall, called RBC-free layer (RBC-FL), as the suspension flows.[22,23] The thickness of RBC-FL is directly associated with blood flow resistance[24-27] and plays a crucial role in the adhesion of leukocytes, platelets, and drug-delivery carriers to vessel walls.[7,15]

The thickness of RBC-FL is governed by a competition between the hydrodynamic lift force acting on RBCs in the direction away from the wall and cell–cell interactions which disperse them and drive them toward the wall.[4,28,29] RBC migration in the regime of low Reynolds (Re) numbers (i.e., negligible inertia) typical for microvascular flow is achieved through RBC dynamics and/or deformations. For instance, a tumbling rigid spheroidal particle in flow without inertia does not experience any directed migration near a wall,[30] but a stable tank-treading motion of a spheroidally shaped membrane (similar to tank-treading RBCs) leads to the migration away from the wall.[31,32] As shown by theoretical analysis,[31,33] experiments[32,34] and simulations,[35] the migration velocity v_l is proportional to $f(C)\dot{\gamma}R^3/d_w^{\alpha}$, where $f(C)$ is a function of the ratio $C=\eta_{in}/\eta_{ex}$ of internal η_{in} and external η_{ex} fluid viscosities, $\dot{\gamma}$ is the local shear rate, R is the characteristic particle size, d_w is the distance away from the wall, and α is an exponent whose value is often reported to be close to two. Similar effects govern the migration of RBCs away from the walls in microvasculature at low Re.[29,35,36]

In microvessels, the lift force on RBCs is counterbalanced by their dispersion due to cell–cell hydrodynamic interactions and volume exclusion in flow.[4,28,37] It is intuitive that fluid flow can significantly enhance such interactions or collisions between suspended particles, which are often referred to as shear-induced dispersion forces and depend on local shear rate, particle size, deformation, and dynamics.[28,32,38] The response of single RBCs to fluid stresses is known to be sensitive to the viscosity ratio C between internal and external fluids.[18,39-41] For example, at low viscosity contrasts $C \lesssim 3$, RBCs tumble at low shear rates and tank-tread at high shear rates,[42-44] while for $C \sim > 3$, the tank-treading motion is suppressed and replaced by dynamic multi-lobed shapes.[18,39] These differences in RBC deformation and dynamics as a function of C are expected to affect the lift force, cell–cell interactions in blood flow, and local structure of RBC suspensions, which influence blood flow resistance. Furthermore, significant alterations in C may occur in different blood diseases and disorders such as sickle-cell anemia[45] and RBC hydration disorders.[46] Under physiological conditions, the viscosity ratio is estimated to be $C \approx 5$ with a cytosol viscosity $\eta_{in} \approx 6$ Pa·s[47] and plasma viscosity $\eta_{ex} \approx 1.2$ Pa·s.[48] For comparison, cytosol viscosity up to 40 Pa·s has been reported in experiments with blood from sickle-cell patients.[45]

The main focus of our investigation is the effect of C on the behavior of RBC suspensions in microvessels and the dependence of RBC-FL thickness and flow resistance on the viscosity contrast. Even though recognized, the importance of $C > 1$ for blood flow is not well studied so far, as most simulation studies of blood flow were performed for $C = 1$.[26,28,49,50] Katanov et al.[28] have investigated the formation of RBC-FL and flow convergence to steady state for $C = 1$, starting from an initially dispersed configuration of RBCs, and found that the full flow convergence requires a length of about $25D$ (D is the tube diameter), which is nearly independent of flow rate, RBC hematocrit, and channel size for 10 μm < D < 100 μm. A recent numerical investigation of blood flow in a tube with a diameter of $D = 70$ μm[51] has predicted a comparable RBC-FL thickness and flow resistance for suspensions with $C=1$ and $C=5$, where the differences become more pronounced at high flow rates. Another simulation study of blood flow in a slit[52] has suggested a domination of the lift force on RBCs over cell–cell interactions for $C=1$, such that a slightly smaller RBC-FL was found for $C=5$ suspension in comparison to $C=1$. To clarify the importance of C for the behavior of RBC suspensions, we have performed a systematic investigation using mesoscopic hydrodynamic simulations, which include suspensions with $C \in [1, 20]$ as well as rigidified RBCs, several different flow rates, hematocrits, and tube diameters. In particular, we investigate the development of RBC-FL for the various conditions, and connect it to the flow resistance, deformation and dynamics of single RBCs. Our results show that the RBC-FL develops faster for $C=1$ in comparison with $C=5$ due to a larger lift force on RBCs with $C=1$. The flow convergence length becomes larger for elevated C values, but remains within approximately $50D$. The RBC-FL thickness for $C=5$ is slightly larger than that for $C=1$, resulting in a nearly negligible effect of C on the flow resistance for vessels with diameters $D > 20\,\mu m$. However, for a larger $D=40\,\mu m$, the flow resistance for $C=5$ is about 10% larger than for $C=1$. A thicker RBC-FL for $C=5$ in comparison to $C=1$ is due to a smaller dispersion of cells, since a larger internal viscosity dampens shape changes and membrane dynamics of RBCs. Suspensions with stiffened RBCs, which approximate the case of $C \to \infty$, exhibit the smallest RBC-FL and the largest flow resistance. The robustness of flow resistance with respect to $C \in [1, 20]$ permits

RBCs to contain a cytosol with a high concentration of hemoglobin, which maximizes oxygen delivery and only moderately affects the flow resistance. Furthermore, an increased viscosity ratio, which may occur in some blood pathologies, likely has a moderate effect on the flow resistance in microcirculation.

The paper is organized as follows. Simulation methods, models, and setup are introduced in Section 2. Section 3 presents simulation results, where the behavior of RBC suspensions with $C \in [1, 20]$ is investigated. The analysis of single-cell characteristics is performed in Sections 3.2 and 3.3, in order to explain differences in blood flow resistance and RBC-FL for various C. Finally, the dependence of flow resistance and RBC-FL thickness on several parameters, including flow rate, tube hematocrit and diameter, is investigated in Section 3.4. Our main results are discussed and summarized in Section 4.

2 | METHODS AND MODELS

Fluid flow is modelled by the smoothed dissipative particle dynamics (SDPD) method[53] with angular momentum conservation,[54] which is a mesoscopic particle-based hydrodynamics approach. The conservation of angular momentum is crucial for the proper representation of cellular motion when distinct fluid viscosities inside and outside the cell are employed.[54] RBCs are represented by a spring-network model,[55-57] and coupled to fluid flow through dissipative forces. The blood flow model with $C = 1$ has already been shown to capture quantitatively the Fahraeus and Fahraeus–Lindqvist effects.[26] Below, we briefly review several model ingredients with an emphasis on the implementation of the viscosity contrast between internal and external fluids separated by the membrane. More details about the methods and models can be found in Refs [28,54,58].

2.1 | RBC membrane model

The RBC membrane is represented by a spring-network model[55-57] with N_v vertices distributed at a biconcave cell shape. Potential energy of the membrane,

$$U_{\text{tot}} = U_{\text{sp}} + U_{\text{bend}} + U_{\text{area}} + U_{\text{vol}},$$

consists of several contributions. U_{sp} corresponds to the spring's energy, which mimics elasticity of the spectrin network attached to the back side of the lipid membrane. U_{bend} is the bending energy, representing bending resistance of the lipid bilayer. U_{area} and U_{vol} impose area and volume conservation constraints, which mimic area incompressibility of the lipid bilayer and incompressibility of a cytosol, respectively. This RBC model has been shown to quantitatively reproduce the viscoelasticity of the RBC membrane, as well as deformation of RBCs due external forces by optical tweezers and under flow.[3,39,57]

The biconcave shape of a RBC at rest is imposed by setting the reduced volume $V^* = 6V_r/\left(\pi D_r^3\right) = 0.64$, where V_r is the RBC volume and $D_r = \sqrt{A_r/\pi}$, with A_r being the area of a RBC. The RBC membrane is characterized by the shear modulus μ and bending rigidity κ, which are implemented through the potential energies U_{sp} and U_{bend}, respectively. The membrane parameters are set to mimic average properties of a healthy RBC with μ = 4.8 μN/m and $\kappa = 70k_BT$. The effective size of a RBC is $D_r = 6.51\,\mu m$, the surface area is $A_r = 132.9\,\mu m^2$, and the total volume is $V_r = 92.45\,\mu m^3$. The stress-free shape of a RBC elastic network is assumed to be an oblate spheroid with a reduced volume of 0.96.

2.2 | Fluid-membrane interactions

To model the viscosity ratio $C = \eta_{\text{in}}/\eta_{\text{ex}} \neq 1$, internal and external fluids have to be separated by the membrane. An impenetrable membrane is implemented through bounce back boundary conditions (BCs) for both internal and external fluid particles at every triangular face of the membrane. Thus, internal fluid particles are subject to bounced back BCs from inside the cell, while external fluid particles are bounced back from the outer membrane surface. Different fluid viscosities are implemented through different friction coefficients of dissipative forces in the SDPD method. Dissipative interactions between internal and external fluids assume the average of the two friction coefficients.

The frictional (dissipative) coupling between fluid and membrane particles is implemented through a dissipative force,[57]

$$\mathbf{f}_{ij}^D = \gamma(1 - r_{ij}/r_m)^\alpha \left(\mathbf{v}_{ij} \cdot \mathbf{e}_{ij}\right) \mathbf{e}_{ij}, \quad r_{ij} = \left|\mathbf{r}_i - \mathbf{r}_j\right| < r_m,$$

similar to that in the dissipated particle dynamics method[59,60] where γ is the friction coefficient, $\alpha = 0.2$ is an exponent of the weight function, r_m is the cutoff radius, $\mathbf{v}_{ij} = \mathbf{v}_i - \mathbf{v}_j$ is the velocity difference, and $\mathbf{e}_{ij} = \mathbf{r}_{ij}/r_{ij}$. The value of γ is computed as,[57]

$$\gamma = \frac{4A_r\eta}{N_v\rho I_V}, \quad I_V = \int_{V_h} (1 - r_{ij}/r_m)^\alpha z dV,$$

where η is the fluid viscosity, ρ is the fluid density, and the volume integral I_V runs over the volume V_h of a half sphere of radius r_m in the positive z direction. This estimation of the friction coefficient assumes a linear flow velocity profile within a distance r_m near the membrane surface, so that the local shear rate cancels out. The cutoff for fluid-membrane coupling is set to $r_m = 0.75\,\mu m$.

To prevent an overlap of two membranes, a short-ranged repulsive Weeks-Chandler-Anderson (WCA) potential is applied between pairs of membrane particles belonging to different cells within the cutoff distance r_{WCA}. Note that the thickness of RBC-FL is slightly sensitive to the choice of r_{WCA}, which depends on membrane resolution. For $N_v = 1000$, the average spring length at rest is approximately $l_{\text{ave}} = 0.4\,\mu m$ and r_{WCA} is set to 0.3 μm to prevent overlap. Doubling the membrane resolution allows a slight decrease of r_{WCA}, which may result in a slight change of the RBC-FL thickness. Nevertheless, $N_v = 1000$ is large enough to properly represent

membrane deformation and nearly eliminate the effect of the cutoff distance r_{WCA} on blood flow properties.

2.3 | Simulation setup

The computational domain is a periodic cylindrical rigid tube with a diameter D and a length $L = 60\,\mu m$ ($\approx 9.2 D_r$), which is long enough to avoid finite-size effects. Initially, RBCs are introduced into the computational domain with an ordered structure. Their number is determined by tube hematocrit H_t (the volume fraction of RBCs in a tube), which is assumed to be $H_t = 30\%$ in most simulations. Note that the tube hematocrit H_t remains constant in simulations, while the discharge hematocrit H_d depends on flow rate, and $H_d \geq H_t$ owing the Fahraeus effect.[19] Then, fluid particles are randomly placed with a uniform distribution into the computational domain. The number density of fluid particles is n = 9μm^{-3}, the smoothing length for SDPD pair interactions is r_c = 1.04 μm, resulting in about 30 particles within the interaction range r_c. The SDPD fluid particles inside the cells represent the internal fluid with viscosity η_{in}, while particles outside the cells correspond to the external fluid with viscosity η_{ex}.

To relax the initially ordered structure of RBCs, the cellular suspension is mixed by applying a flow within the tube, which is driven by a force exerted on all fluid particles. When the cells are well mixed, the flow is stopped, and the RBCs are let to diffuse and fill up the whole tube, resulting in a fully dispersed RBC configuration as illustrated in Figure 1A. After the dispersed cell configuration is reached, a constant force f applied on all fluid particles in the x direction is turned on again to drive the fluid flow. This driving force represents a constant uniform pressure gradient $\frac{\Delta P}{L} = n \cdot f$ (ΔP is the pressure drop over the length L), while the flow rate adapts to simulated blood flow conditions. The generated flow leads to RBC migration away from the wall and the formation of a denser cellular region near the tube center, as shown in Figure 1B,C for two different C values.

Note that a fully dispersed initial RBC distribution within the tube represents the worst-case scenario for flow resistance, and the longest convergence length required for blood flow to fully develop. In microcirculation, vessel bifurcations and branches result in the dispersion of RBCs, whose distribution likely lies between the well-dispersed RBC configuration we employ and the distribution of RBCs in fully developed flow. We would like to emphasize that our setup does not capture the intricate flow inhomogeneities at a tube entry or after a vessel bifurcation, which can further affect the convergence length.

The flow strength is characterized by the dimensionless capillary number

$$\mathrm{Ca} = \frac{\eta_{ex}\bar{\dot{\gamma}}}{\mu/D_r} = \bar{\dot{\gamma}}\tau,$$

which represents the ratio between fluid stresses and elastic membrane stresses. Here, $\bar{\dot{\gamma}} = \bar{v}/D$ is the average shear rate (or pseudo-shear rate) with the average velocity $\bar{v}$ for a Newtonian fluid with viscosity η_{ex} driven by the same pressure gradient. Thus, the capillary number directly characterizes the applied driving force or the pressure gradient. Note that $\tau = \eta_{ex} D_r/\mu$ represents a characteristic relaxation time of a RBC, which is equal to approximately 1.6 × 10^{-3} s for μ = 4.8 μN/m and blood plasma viscosity η_{ex} = 1.2 mPa·s. Simulations are performed at low enough Reynolds numbers, such that the largest investigated flow rate corresponds to $\mathrm{Re} = \rho \bar{v} D_r/\eta_{ex} = 2.6$ (ρ is the fluid density). Several tests have been performed to verify that inertia has a negligible effect on the results for blood flow resistance and RBC-FL thickness in the regime of used Re numbers. Furthermore, the Mach number $\mathrm{Ma} = \bar{v}/c_s$ with the speed of sound c_s is <0.15 in all simulations, such that the fluid flow can be considered incompressible.

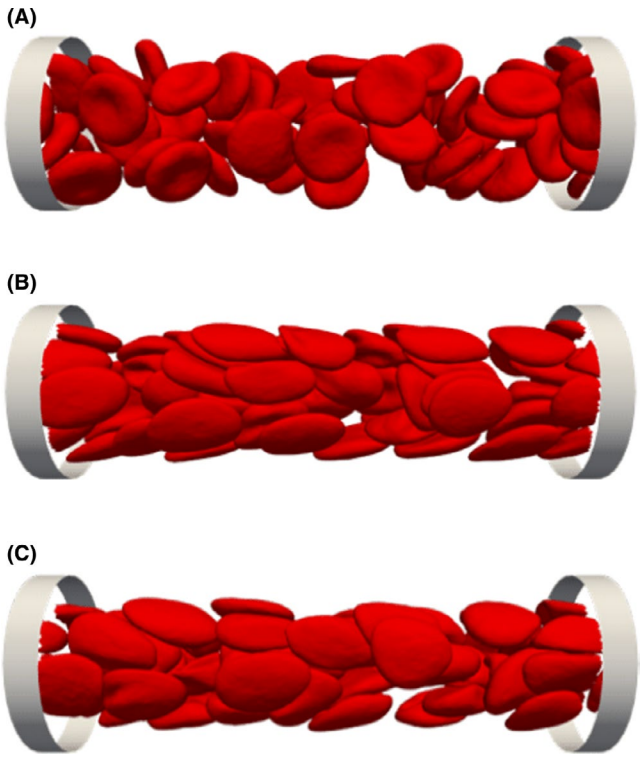

FIGURE 1 Simulation snapshots for D = 20 μm and $H_t = 30\%$. (A) Configuration of dispersed RBCs, before the flow is applied. (B) Converged flow of a RBC suspension for $C = 1$ and $\mathrm{Ca} = 0.61$ ($\bar{\dot{\gamma}} = 377.4\,s^{-1}$). (C) Converged flow for $C = 5$ and the same Ca as in (b). The flow is from left to right [Colour figure can be viewed at wileyonlinelibrary.com]

Solid wall BCs are modelled by a layer of immobile SDPD particles with a width r_c. The structure and density of the wall layer are identical to those of equilibrated SDPD fluid particles. The pair forces between fluid and wall particles are the same as those for fluid–fluid interactions. Furthermore, an adaptive shear force is added to fluid particles within a near-wall layer of thickness r_c to fully ensure no slip conditions.[61] To prevent wall penetration, both fluid and membrane particles are reflected back inside the tube domain.

3 | RESULTS

3.1 | Development of the flow and RBC-FL

To examine flow development for various viscosity contrasts $C \in [1, 20]$, the viscosity of internal fluid η_{in} is varied. This range of C covers RBC physiological conditions as well as some diseased states. This range of C covers RBC physiological conditions with $C \approx 5$[47] as well as some blood diseases such as sickle-cell anemia with C values up to 30.[45] After the pressure gradient is applied, the flow develops and reaches a terminal velocity profile with a position-averaged velocity v_T at long times. Note that the velocity of individual cells depends on their location within the tube and can fluctuate in time even after the average flow velocity has reached steady state. v_T is inversely proportional to the flow resistance, and can be used to obtain the relative suspension viscosity $\eta_{rel} = \bar{v}/v_T$, which compares the volumetric flow rate of RBC suspension with that of external fluid (without RBCs) for the same pressure gradient. Thus, η_{rel} quantifies an increase in the flow resistance due to the presence of RBCs. The dependence of η_{rel} on C for a fixed tube hematocrit of $H_t = 30\%$ but varying discharge hematocrit H_d is shown in Table 1. Interestingly, the relative viscosity increases only by about 8% when C is increased 20 times. Furthermore, Table 1 also shows η_{rel} = 1.7 for a suspension of stiffened cells (SC), whose shear modulus μ is 100 times larger than that of healthy RBCs. Stiffened RBCs do not exhibit significant deformation in fluid flow and represent a limit of very large viscosity contrast. Furthermore, the case of stiffened RBCs is relevant for some pathological conditions, e.g. the shear modulus of infected RBCs in malaria can increase up to ten times.[62,63]

As the flow develops, RBCs migrate toward the tube center, resulting in the formation of RBC-FL near the wall whose thickness is directly associated with the flow resistance. To measure the thickness of RBC-FL, RBC suspension at a fixed time is projected onto the y-z plane,[26] which is similar to taking a snapshot from experimental movie.[64] Then, distances between the tube wall and projected RBC-core edge are extracted at several positions along the tube. Averaging these distances yields an average thickness of the RBC-FL δ. To improve RBC-FL statistics, we also employ flow axisymmetry, such that the thickness is sampled for 10 different angles by rotating a simulated configuration before the projection onto the y-z plane is performed. Furthermore, the RBC-FL data are accumulated over a certain time window, which is chosen long enough to avoid large deviations in RBC-FL thickness measurements and short enough to resolve the dynamics of RBC-FL development. This time window corresponds to about 8 ms, within which RBCs move on average 3 μm.

The RBC-FL thickness for the initial configuration without flow (Figure 1A) is $\delta \approx 2.2\,\mu m$. This non-zero RBC-FL thickness is due to finite tube hematocrit $H_t = 30\%$, the biconcave RBC geometry, which affects cell close-packing, and entropic repulsion from the wall that originates from the rotational diffusion of RBCs. Figure 2 shows the development of RBC-FL as a function of the average flow convergence length $L_e = \bar{v}t$. At short times ($L_e < 5D = 100\,\mu m$), δ increases faster for the suspension with C = 1 than for those with C > 1, see Figure 2A. However, the RBC-FL thickness for C = 1 suspension saturates at a smaller value than δ for C > 1 with a difference of about 200–300 nm, as shown in Figure 2B. As C increases from 5 to 20, the converged RBC-FL thickness shows a similar plateau value of $\delta \approx 3.1\,\mu m$. Converged or final RBC-FL thicknesses δ_f for different C values are given in Table 1. For the SC suspension with stiffened RBCs, δ fluctuates within the range of 2.0–2.3 μm, which is close to the RBC-FL thickness without flow. The differences in RBC-FL thicknesses for various C values are due to cell deformation and dynamics in flow, which will be discussed later. The critical convergence length L_e^c required for the development of RBC-FL is close to 25D (i.e., $L_e^c \approx 500\,\mu m$ here) for both C = 1 and C = 5 suspensions, which is consistent with the previous investigation for C = 1.[28] Nevertheless, L_e^c becomes longer with increasing C, as L_e^c is approximately 50D for C = 20. The decrease of δ from its initial thickness for the SC suspension makes it difficult to define L_e^c due to a weak migration strength in this case. The development and dependence of RBC-FL thickness on C is determined by the migration and interactions between RBCs as cellular core forms.

3.2 | Structure and mobility of the flowing RBC suspension

The RBC-FL and cellular core are governed by a balance of hydrodynamic lift forces that drive RBCs away from the wall and cell–cell collision interactions within the cellular core that disperse RBCs.[28] Therefore, to better understand the dependence of final RBC-FL thickness δ_f on the viscosity contrast, it is instructive to take a look at the structural properties of RBC suspensions after the flow has fully developed. The distribution of RBCs within the tube can be characterized by local hematocrit $H_t(r)$ obtained from simulations through spatial averaging of the density of fluid particles inside RBC membranes. Figure 3A shows the normalized local hematocrit $H_t(r)/H_t$ within the tube for various viscosity contrasts. All $H_t(r)$ distributions contain a depletion zone near the wall, whose thickness is directly associated with δ_f. For instance, the difference in δ_f can clearly be seen for C = 1, C = 5 and SC suspensions. Inside the RBC-rich region, $H_t(r)$ is nearly uniform with a small peak near the center, which is typical for small tube diameters.[27] For $C \geq 5$, the $H_t(r)$ distributions are nearly independent of the viscosity contrast.

Radial cell density can also be characterized by the distribution of RBC centers of mass denoted as COM(r) and shown in Figure 3B. COM distributions have a peak near the RBC-FL. As the tube center is approached, COM(r) first decreases and then slightly increases for both C = 1 and C = 5 suspensions. As C is increased, spatial inhomogeneity in COM distribution becomes stronger. This is related to the RBC dynamics in flow and a decrease in radial migration of RBCs with increasing C, which will be discussed later. The SC suspension shows the strongest variations in COM(r), which is consistent with the $H_t(r)$ distribution in Figure 3A.

TABLE 1 Relative suspension viscosity η_{rel}, final RBC-FL thickness δ_f, and discharge hematocrit H_d as a function of C. Here, tube hematocrit $H_t \sim 30\%$ is fixed, D = 20 μm, and $Ca = 0.61$ ($\bar{\dot{\gamma}} = 377.4\,s^{-1}$). "SC" denotes stiffened cells, whose shear modulus is increased 100 times in comparison to that of a healthy RBC

Viscosity contrast (C)	1	5	10	20	SC
η_{rel}	1.27	1.30	1.33	1.37	1.70
δ_f [μm]	2.77	3.12	3.05	3.14	2.09
H_d, ($H_t = 27.5\%$)	33.1%	33.4%	33.1%	33.0%	31.0%

Figure 4A presents flow velocity profiles $v(r)$ normalized by the average velocity $\bar{v}$ for different RBC suspensions and blood plasma (i.e., for a Newtonian fluid). All velocity profiles for RBC suspensions are flattened at the tube center due to the presence of the cellular core. The velocity profiles do not exhibit large differences for various C values and overlap with the Newtonian fluid case only in the RBC-FL. An increase of C results in slight flattening of $v(r)$ near the tube center. Figure 4B shows radial profiles of local shear rates $\dot{\gamma}(r)$ normalized by the wall shear rate $\dot{\gamma}_w = 8\bar{\dot{\gamma}}$, which are computed from the velocity profiles $v(r)$ in Figure 4A. Inside the cellular core, $\dot{\gamma}(r)$ for all RBC suspensions is close to zero (i.e., plug flow) and much less than that for the Newtonian case. Within the RBC-FL, $\dot{\gamma}(r)$ quickly increases from nearly zero to the wall shear rate. The SC suspension exhibits a steeper increase in $\dot{\gamma}(r)$ within the RBC-FL in comparison to soft-RBC suspensions.

Even though fully developed velocity profiles are stable, RBCs within the cellular core are mobile, as can be seen from the trajectories of selected individual cells in Figure 5A. Thus, cells can migrate between different fluid layers laterally, even after the RBC-FL has fully developed ($L_e > 50D$). To characterize the lateral mobility of RBCs, we define a dimensionless lateral mobility coefficient $R_T = |\Delta r_{com}| / \Delta x_{com}$, where the absolute value of the cell velocity in radial direction, $\Delta r_{com}/\Delta t$, is normalized by its translational velocity along the x direction, $\Delta x_{com}/\Delta t$ (here $\Delta t \approx 8$ms). $R_T(r)$ is shown in Figure 5B and can be interpreted as a measure of cell–cell collisions. $R_T(r)$ remains nearly constant within the cellular core and decreases slightly near the RBC-FL. Interestingly, $R_T(r)$ or fluctuations in lateral cell motion become smaller as C increases, leading to less dispersion within the cellular core and a thicker RBC-FL. Nevertheless, a large enough increase in C should eventually lead to an increase in $R_T(r)$, as for the SC suspension, where $R_T(r)$ values are slightly larger than those for C = 1. For comparison, we have also performed simulations of a single RBC migrating from the wall to the tube center for C = 1 and C = 5 (the dashed lines in Figure 5B). For a single cell, lateral migration due to the hydrodynamic lift force near the wall is much faster than that in a suspension, because cell–cell collisions are not present. However, in the tube center, cell–cell interactions within RBC suspensions enhance lateral migration of cells in comparison to the case of a single RBC.

Note that $R_T(r)$ of a single RBC for C = 1 in Figure 5B is larger than for C = 5, indicating a stronger lateral migration. Figure 6 presents the lift velocity v_l of a single migrating RBC normalized by local shear rate $\dot{\gamma}(r)$ for $C \in [1, 10]$. Clearly, the RBC with C = 1 migrates faster than that with C = 5. This result is consistent with previous simulation studies,[35,65] where the lift velocity on single RBCs in pure shear flow has been found to decrease with increasing C. The ratio $v_l/\dot{\gamma}(r)$ is expected to be proportional to $1/d_w^{\alpha}$, where d_w is the distance from the wall. We find that $\alpha \simeq 2$ for $C \le 2$, and $1 < \alpha < 2$ for C = 5, in agreement with experimental measurements.[32,34,66] For the RBC with C = 10, α is nearly zero. Note that these simulations are performed in a tube with diameter D = 20 μm ($D_r/D = 0.33$), representing a rather strong confinement with varying local shear rates. Furthermore, initial cell migration might be affected by the flow development, as we start from the no-flow condition.

The faster migration velocity of RBCs for C = 1 in comparison with C = 5 is due to differences in cell dynamics for different C. At high enough shear rates (e.g., near the wall), RBCs generally exhibit a tank-treading-like motion with a preferred alignment in flow for C = 1, while a tumbling-like dynamics with multi-lobed shapes is found for C = 5.[18,39] The tank-treading dynamics of RBC membrane near a wall leads to a larger lift force than for the tumbling dynamics.[30,31] Note that the slower migration velocity of RBCs for C = 5 in comparison to C = 1 is consistent with a slower development of the RBC-FL for C = 5 in Figure 2A.

3.3 | Shape and dynamics of single cells inside the RBC-core

RBC crowding and dynamics inside the cellular core determine cell–cell dispersive interactions that affect the thickness of RBC-FL. In

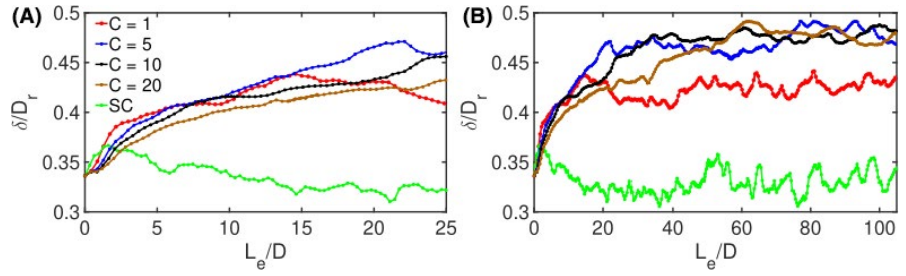

FIGURE 2 Evolution of the RBC-FL thickness in flow as a function of average convergence length $L_e = \bar{v}t$ for C = 1, 5, 10, 20 and a suspension of stiffened RBCs (denoted SC). (A) Transient behavior at the beginning of RBC-FL development. (B) Dynamics of the RBC-FL thickness over the total simulation time. $H_t = 30\%$, D = 20 μm, and $Ca = 0.61$ ($\bar{\dot{\gamma}} = 377.4\,s^{-1}$) [Colour figure can be viewed at wileyonlinelibrary.com]

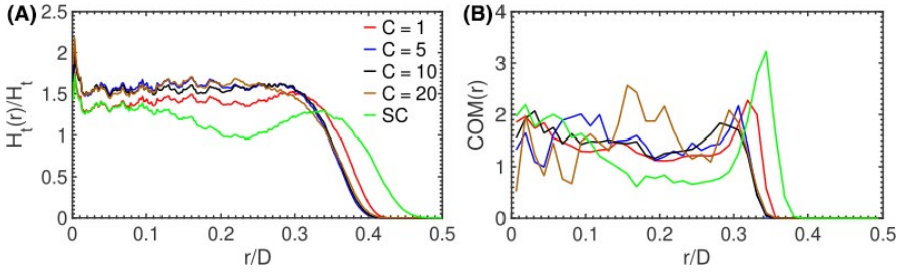

FIGURE 3 RBC distribution as a function of radial position within the tube. (A) Local hematocrit $H_t(r)/H_t$ profile for C = 1, 5, 10, 20 and SC suspensions. (B) Center of mass (COM) distribution of RBCs. The data are collected after the flow has fully developed for $L_e > 50D$. $H_t = 30\%$, D = 20 μm, and $\mathrm{Ca} = 0.61$ ($\bar{\dot{\gamma}} = 377.4\,\mathrm{s}^{-1}$) [Colour figure can be viewed at wileyonlinelibrary.com]

particular, RBCs in flow show frequent changes in the shape, orientation, and membrane tank-treading motion, which often cannot be decoupled completely. Figure 7 shows several representative snapshots of RBCs near the RBC-FL and in the tube center. To better understand the behavior of single RBCs within the cellular core, we look at several cell characteristics. Shape changes of RBCs are quantified by the asphericity $A = \left[(\lambda_1-\lambda_2)^2+(\lambda_2-\lambda_3)^2+(\lambda_1-\lambda_3)^2\right] / \left(2R_g^4\right)$, where $R_g^2 = \lambda_1+\lambda_2+\lambda_3$ is the gyration radius squared and $\lambda_1 \le \lambda_2 \le \lambda_3$ are the eigenvalues of the gyration tensor. For a biconcave RBC shape at rest, A = 0.15, while A = 0 corresponds to a sphere and A = 1 to a long thin rod. For example, the largest eigenvalue λ_3 can be interpreted as the extension of a RBC in the flow direction (λ_3 = 4.77 μm for a RBC at rest).

Figure 8A shows that RBCs are significantly stretched in most locations within the cellular core region, except near the tube center. Close to the center, different shapes with A < 0.15 are generally observed (Figure 8B), whose representative snapshots are shown in Figure 7. Both λ_3 and A in Figure 8 increase nearly linearly from the tube center to the RBC-FL. At the edge of the cellular core, elongated slipper shapes prevail, as shown in Figure 7. SC cells show a crumpled configuration, which is due to not only fluid flow stresses, but also residual elastic stresses within the membrane, since the RBC stress-free shape corresponds to an oblate spheroid with a reduced volume of 0.96 and the SC cells have a high shear modulus. Therefore, stiffened cells even without flow show some degree of membrane roughness in comparison with the smooth surface of soft RBCs. Nevertheless, the overall rest shape of SC cells remains biconcave. The shape characteristics of SC cells in Figure 8 are nearly independent of the radial position within the tube, indicating that cell deformation can nearly be neglected. As C increases from 1 to 5, λ_3 decreases and its slope reduces as well, indicating that RBCs at C = 5 are stretched less than those at C = 1. Suspensions with C > 5 show similar shapes as those for C = 5. In comparison to RBCs in a suspension, single cells in tube flow have a larger (smaller) elongation than for C = 1 (C = 5).

In addition to deformation in flow, cell orientation changes and membrane exhibits a tank-treading motion. To quantify RBC orientation with a varying shape, we include in the analysis only the shapes with an asphericity larger than that of a biconcave shape at rest (A > 0.15), where a well-defined axis from the eigenvector $\overrightarrow{v_1}$ corresponding to λ_1 can always be obtained. $\overrightarrow{v_1}$ often does not lie within the flow velocity gradient plane, due to cell–cell interactions and complex cell relaxation under fluid stresses. To simplify the quantification of cell dynamics, we define an inclination angle θ (marked in red in Figure 9) as the angle between the vector $\overrightarrow{v_1}$ and the flow direction x within the flow velocity gradient plane (i.e. within $x-\overrightarrow{r_c}$ plane, where $\overrightarrow{r_c}$ is the vector from the tube central axis to the cell's center of mass). Figure 10A shows θ as a function of cell position in the flow direction for one selected cell from each suspension. θ may frequently exhibit discontinuous jumps of 180 degrees due to the symmetric disk-like rest shape, so that even small deformations can cause a reversal of the $\overrightarrow{v_1}$ vector. Despite these jumps, RBC tumbling in the SC suspension can clearly be identified from the green trajectories in Figure 10A. Tumbling motion is infrequent for soft-RBC suspensions, where jumps between +90° and −90° are found instead and the departure of θ from these two values is generally within 30°. Rare tumbling of RBCs for C = 20 suspension can be seen by the brown line in Figure 10A, but the tumbling period is extremely

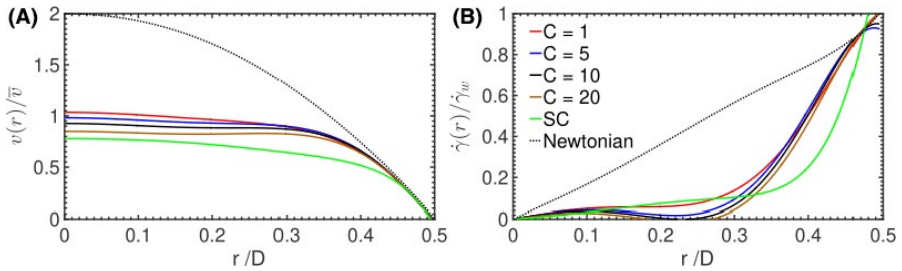

FIGURE 4 (A) Normalized velocity profile $v/\bar{v}$ and (B) local shear rate $\dot{\gamma}(r)/\dot{\gamma}_w$ as a function of radial position within the tube for various RBC suspensions. $H_t = 30\%$, D = 20 μm, and $\mathrm{Ca} = 0.61$ ($\bar{\dot{\gamma}} = 377.4\,\mathrm{s}^{-1}$) [Colour figure can be viewed at wileyonlinelibrary.com]

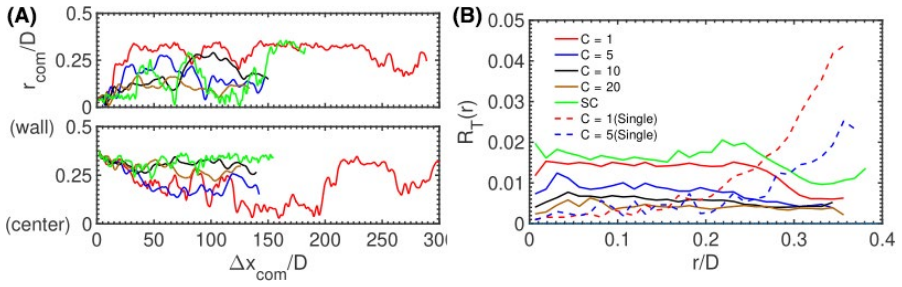

FIGURE 5 Characteristics of RBC mobility perpendicular to the flow direction. (A) Trajectories of selected individual cells whose initial positions are closer to the tube center (top) and closer to the wall (bottom). (B) Distributions of the dimensionless lateral mobility coefficient $R_T(r)$ as a function of radial position within the tube. $H_t = 30\%$, D = 20 μm, and $Ca = 0.61$ ($\bar{\dot{\gamma}} = 377.4\,s^{-1}$) [Colour figure can be viewed at wileyonlinelibrary.com]

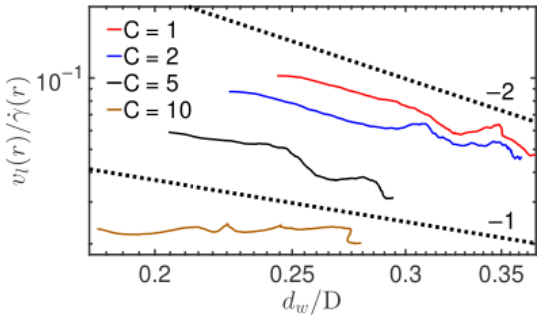

FIGURE 6 Lift velocity v_l normalized by local shear rate $\dot{\gamma}(r)$ for a single RBC migrating away from the wall as a function of the distance d_w from the wall to the cell's COM in tube flow with D = 20 μm. Dashed lines indicate the power-law functions of d_w^{-1} and d_w^{-2} in the log-log plot [Colour figure can be viewed at wileyonlinelibrary.com]

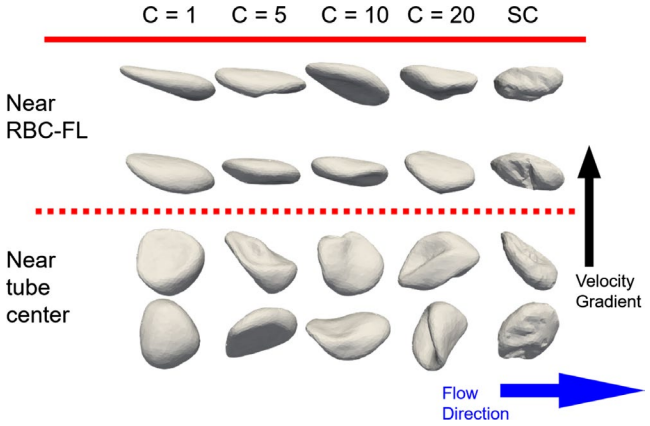

FIGURE 7 Representative snapshots of RBC shapes near the edge of the cellular core and in the tube center for different RBC suspensions. Each column denotes a specific C value. $H_t = 30\%$, D = 20 μm, and $Ca = 0.61$ ($\bar{\dot{\gamma}} = 377.4\,s^{-1}$) [Colour figure can be viewed at wileyonlinelibrary.com]

long (>120D). Thus, cell–cell interactions in a crowded environment strongly hinder solid-like tumbling motion and RBCs are forced to relax fluid stresses via shape deformation instead. Note that RBC tumbling is expected to result in a stronger dispersion effect within the cellular core than the tank-treading motion.

The average orientation angle of RBCs as a function of radial position can be tracked through the absolute value of $|\bar{\theta}|$, as shown in Figure 10B. Near the RBC-FL, the average angle $\bar{\theta}$ approaches 90°, so that RBCs are aligned along the flow direction. $\bar{\theta}$ decreases toward the tube center, and near the center the orientation angle is often not well defined as RBCs attain shapes with $A < 0.15$. The average angle $\bar{\theta}$ for $C \geq 5$ is slightly larger than for $C = 1$, indicating that RBCs are more aligned with the flow for large C values, which can also be seen in Figure 7.

Strong dynamic changes in RBC shape significantly complicate cell orientation analysis and do not always allow decoupling between tumbling motion with shape rotation and tank-treading motion with membrane circulation. To analyze relative membrane motion, we monitor the material angle θ_M defined as the angle between the material vector $\overrightarrow{r_M}$ and the flow direction, see Figure 9. Note that we cannot fully distinguish between tank-treading and tumbling motion by using θ_M. Changes in θ_M for a selected RBC are shown in Figure 11A for various viscosity contrasts. θ_M exhibits a nearly monotonic increase as the RBC goes forward. For $C = 1$, a smooth dependence of θ_M is observed, indicating continuous tank-treading motion of the membrane. For $C \geq 5$, an increase in θ_M is slower than for $C = 1$, and membrane rotation shows short frequent pauses followed by periods of rapid θ_M increase for SC suspension.

Membrane motion can be quantified further by an average change in θ_M as RBCs flow, which is defined as the ratio $\Delta\theta_M/\Delta x_{com}$ between the change in θ_M and the corresponding change in x_{com} calculated for a fixed time interval $\Delta t \approx 8$ms. Figure 11B presents $\Delta\theta_M/\Delta x_{com}$, where the rotation tendency is most prominent near the RBC-FL and decreases toward the tube center. A slight enhancement of $\Delta\theta_M/\Delta x_{com}$ can be observed near the tube center. Large C values suppress membrane rotation, since a large difference in $\Delta\theta_M/\Delta x_{com}$ is observed between $C = 1$ and $C = 5$ suspensions. The dependence of $\Delta\theta_M/\Delta x_{com}$ is similar for all $C \geq 5$ suspensions. In comparison to single-cell dynamics in tube flow, the membrane rotation for cell suspensions is suppressed by surrounding cells.

3.4 | Dependence of the RBC-FL thickness on other flow parameters

To study the dependence of RBC-FL thickness on other flow parameters, we compare suspensions with C = 1 and C = 5 for different flow conditions $\mathrm{Ca} \in [0.06, 0.61]$ ($\bar{\dot{\gamma}} \in [37, 378]\ \mathrm{s}^{-1}$), hematocrits $H_t \in [20, 45]$ %, and tube diameters $D \in [10, 40]\ \mu m$. Table 2 presents relative viscosity η_{rel} and final RBC-FL thickness δ_f for various Ca, where η_{rel} increases as Ca decreases. Furthermore, η_{rel} for $C = 5$ suspension is only slightly larger than η_{rel} for C = 1 suspension and the difference is most prominent at intermediate flow rates. The converged RBC-FL thickness δ_f decreases as the flow slows down. The C = 1 suspension has a smaller RBC-FL thickness than the C = 5 suspension with a difference of about 350 nm at Ca = 0.61 and about 100 nm at Ca = 0.06.

Table 3 shows that η_{rel} increases as H_t increases. η_{rel} for C = 5 is slightly larger than for C = 1, and the difference in η_{rel} caused by C is most prominent for dense suspensions. The development of RBC-FL for different H_t values is shown in Figure 12, where δ_f decreases for increasing H_t, consistently with the increase of η_{rel}. δ_f values for C = 5 are slightly larger than those for C = 1, in agreement with already discussed results.

Finally, we investigate the dependence of η_{rel} and δ_f on vessel diameter D at $H_t = 30\%$. Table 4 shows that η_{rel} decreases as D decreases which is consistent with the Fahraeus-Lindqvist effect.[20] η_{rel} is quite insensitive to C for $D \leq 20\mu m$; however, η_{rel} is about 10% larger for C = 5 in comparison to C = 1 for $D = 40\mu m$. Consistently, δ_f increases as D increases, as shown in Figure 13. This trend may depend on Ca, which affects dynamics of RBCs near the RBC-FL. The difference between C = 1 and C = 5 suspensions is similar for $D = 40\mu m$ and $D = 20\ \mu m$, but nearly disappears for $D = 10\mu m$.

4 | SUMMARY AND DISCUSSION

The main focus of our study is the effect of the viscosity ratio $C = \eta_{in}/\eta_{ex}$ on the behavior of RBC suspensions in microvessels in order to understand the importance of C for microvascular blood flow. Interestingly, for small vessel diameters $D \leq 20\mu m$, $C \in [1, 20]$ has a weak effect on the resistance of converged flow quantified by the relative viscosity η_{rel}. For $D = 20\mu m$, when C increases from 1 to 5, the change in η_{rel} is within 2%, and a further increase of C from 5 to 20 leads to an increase of η_{rel} by about 6%. Nevertheless, for larger vessel diameters the effect of C on flow resistance is more pronounced, as η_{rel} for $C = 5$ is about 10% larger than that for $C = 1$ in case of $D = 40\mu m$. To explain these differences in flow resistance, we have systematically analyzed the RBC-FL thickness and its relation to cell deformation and dynamics in flow.

The development of RBC-FL is governed by the two main mechanisms:[28] (i) RBC migration away from the wall due to the hydrodynamic lift force and (ii) the dispersion of RBCs within the cellular core due to cell–cell interactions in flow. The migration of RBCs away from the wall can be attributed to their shape deformation and membrane dynamics. For instance, RBCs with $C = 1$ migrate faster than those with $C = 5$, which is consistent with a slower development of the RBC-FL for $C = 5$ in Figure 2A. This results from the fact that both shape deformation and membrane dynamics are suppressed as C increases from 1 to 5, since a larger internal viscosity dampens RBC shape changes and dynamics. The importance of cell deformability for migration and the formation of RBC-FL is further illustrated by the results for SC suspension. Stiffened RBCs exhibit tumbling dynamics, which leads to a weak lift force, small RBC-FL thickness, and a large flow resistance.

The dispersion of RBCs within the cellular core counterbalances the lift force and is governed by local shear rate, shape deformations, and membrane dynamics. Both shape deformations and membrane dynamics are attenuated for $C = 5$ in comparison to $C = 1$. For example, the shape asphericity A for $C = 5$ is smaller than for $C = 1$, indicating that RBCs are less stretched. Furthermore, membrane dynamics for $C = 5$ is slower than for $C = 1$, because membrane tank-treading is more pronounced for the low viscosity contrast. This leads to a weaker hydrodynamic repulsion between RBCs in the $C = 5$ suspension, whose origin is similar to the lift force near a wall. To further confirm that the dispersion of RBCs is larger for $C = 1$ than for $C = 5$, we have performed several simulations of the collision of two cells in tube flow. After subtracting the migration effect, we find that the collision of two RBCs leads to a larger change in lateral cell displacement for $C = 1$ than for $C = 5$, indicating a stronger dispersion effect for $C = 1$. Even

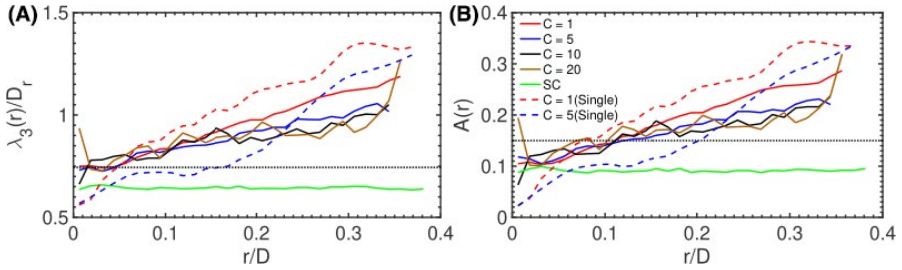

FIGURE 8 Characterization of RBC shapes in blood flow. (A) The largest eigenvalue λ_3 of the gyration tensor, showing relative RBC stretching in the cellular core. (B) Cell asphericity A. Different colors mark different RBC suspensions. The horizontal dashed line corresponds to the RBC shape at rest. The red and blue dashed lines represent the shapes of a single cell in tube flow. $H_t = 30\%$, D = 20 μm, and $\mathrm{Ca} = 0.61$ ($\bar{\dot{\gamma}} = 377.4\ \mathrm{s}^{-1}$) [Colour figure can be viewed at wileyonlinelibrary.com]

though cell collisions in dense suspensions involve more complex multicellular interactions, the lateral mobility coefficient R_T in Figure 5B is smaller for $C=5$ than for $C=1$, which is consistent with the simulations of binary collisions. Therefore, the cellular core for $C=5$ remains more compactly packed than for $C=1$, which is documented by a slightly thicker RBC-FL. The importance of RBC dynamics in flow is further emphasized by the behavior of stiffened RBCs. Hardened cells exhibit tumbling dynamics even in the cellular core, which results in their significant dispersion within the tube and a thin RBC-FL.

With the two mechanisms at hand, differences in flow resistance for various conditions can be rationalized. Despite the fact that the effective viscosity of the RBC-core for $C \geq 5$ is larger than for $C=1$, the flow resistance is nearly independent of C for $D \leq 20\mu m$. This is due to a larger RBC-FL thickness δ_f (by about 10%–15% or approximately 300 nm) for $C \geq 5$ in comparison to $C=1$, which compensates the larger effective viscosity of the RBC-core, such that the overall flow resistance remains nearly independent of C. The flow resistance in capillary-size (i.e. $D \approx 10\mu m$) vessels is weakly affected by C, because RBCs mainly form a single-cell train,[67] resulting in a reduction of the cell–cell dispersion effect and nearly no difference in RBC-FL for $C \in [1, 20]$. For larger vessel diameters ($D > 20\mu m$), η_{rel} for $C \geq 5$ can be noticeably larger than that for $C=1$ because the differences in RBC-FL thickness on the order of 300 nm cannot fully counterbalance the larger effective viscosity of the RBC-core for $C \geq 5$ in comparison to $C=1$. Therefore, the effect of C on the flow resistance is expected to become more pronounced as the vessel diameter is increased.

The dependence of the converged RBC-FL thickness δ_f on the flow rate is consistent with the discussion of cell deformation and dynamics above, such that a decrease in driving pressure gradient weakens cellular dynamics and the exerted lift force, resulting in a reduction of δ_f and an increase of flow resistance. Thus, the flow resistance is expected to be larger in the venular part of microvasculature (with $\bar{\dot{\gamma}} \leq 100\,s^{-1}$ or $Ca \leq 0.16$), where blood flow velocities are significantly smaller than those in the arteriolar part of the microvasculature ($\bar{\dot{\gamma}} \geq 100\,s^{-1}$ or $Ca \geq 0.16$).[1,68] As expected, an increase in hematocrit leads to a decrease of δ_f due to increased cell crowding, accompanied also by a slightly attenuated RBC dynamics. Note that the difference in η_{rel} between $C=1$ and $C=5$ is more pronounced for $H_t=45\%$ than for smaller H_t values. However, the difference in η_{rel} at $H_t=45\%$ is likely of limited relevance for

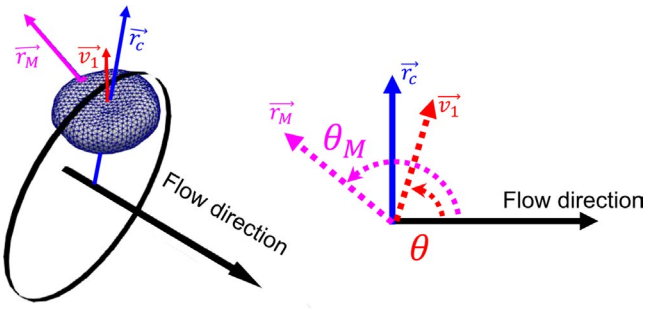

FIGURE 9 Definition of the inclination angle θ and the material angle θ_M. Eigenvector $\vec{v_1}$ of the gyration tensor (red arrow), the vector $\vec{r_c}$ from the tube central axis to the cell's center of mass (blue arrow), and the material vector $\vec{r_M}$ from the cell's center of mass to a specific material point (pink arrow) are shown

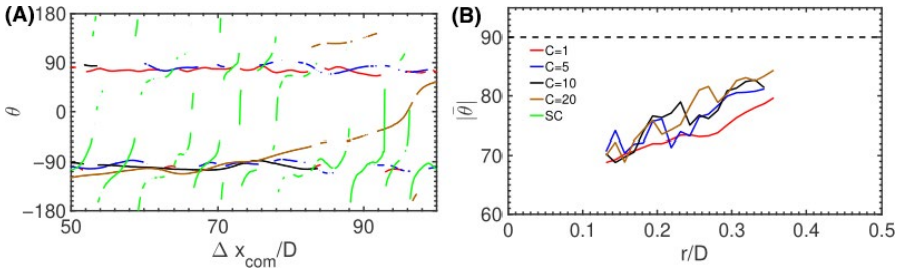

FIGURE 10 (A) Orientation angle θ of a selected cell as a function of RBC displacement. (B) Dependence of the average inclination angle $|\bar{\theta}|$ on the radial position within the tube flow. Different suspensions are represented by different colors: $C=1$ (red), $C=5$ (blue), $C=10$ (black), $C=20$ (pink), and SC suspension (green). $H_t=30\%$, D = 20 μm, and $Ca=0.61$ ($\bar{\dot{\gamma}}=377.4\,s^{-1}$) [Colour figure can be viewed at wileyonlinelibrary.com]

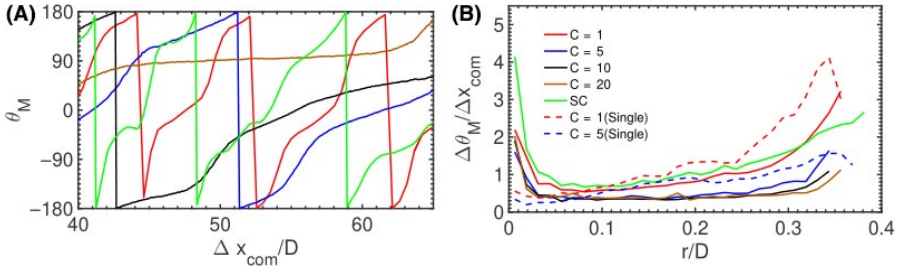

FIGURE 11 RBC membrane motion characterized by θ_M. (A) θ_M evolution for a single selected RBC in flow. (B) Average change in θ_M obtained as the ratio $\Delta\theta_M/\Delta x_{com}$ as a function of r. $H_t=30\%$, D = 20 μm, and $Ca=0.61$ ($\bar{\dot{\gamma}}=377.4\,s^{-1}$) [Colour figure can be viewed at wileyonlinelibrary.com]

TABLE 2 Relative viscosity η_{rel}, final RBC-FL thickness δ_f, and discharge hematocrit H_d for various flow conditions characterized by Ca. D = 20 μm and $H_t = 30\%$

Ca	0.61	0.31	0.14	0.06
$\eta_{rel}^{C=1}$	1.27	1.33	1.46	1.79
$\eta_{rel}^{C=5}$	1.30	1.41	1.53	1.86
$\eta_{rel}^{C=5}/\eta_{rel}^{C=1} - 1$	2.15%	6.25%	4.61%	3.50%
$\delta_f^{C=1}$ [μm]	2.77	2.79	2.66	2.42
$\delta_f^{C=5}$ [μm]	3.12	2.90	2.72	2.50
$H_d^{C=1}$	33.1%	33.0%	32.7%	31.8%
$H_d^{C=5}$	33.4%	32.9%	32.3%	31.7%

TABLE 3 Relative viscosity η_{rel}, final RBC-FL thickness δ_f, and discharge hematocrit H_d for various tube hematocrits H_t. D = 20 μm and $Ca = 0.61$ ($\bar{\dot{\gamma}} = 377.4\,s^{-1}$)

H_t	20%	30%	45%
$\eta_{rel}^{C=1}$	1.13	1.27	1.72
$\eta_{rel}^{C=5}$	1.16	1.30	1.87
$\eta_{rel}^{C=5}/\eta_{rel}^{C=1} - 1$	2.59%	2.15%	9.09%
$\delta_f^{C=1}$ [μm]	1.45	2.77	3.65
$\delta_f^{C=5}$ [μm]	1.65	3.12	3.88
$H_d^{C=1}$	25.4%	33.1%	49.9%
$H_d^{C=5}$	25.3%	33.4%	49.6%

microvascular flow, because characteristic tube hematocrits in the microcirculation are generally smaller than 35%,[1,68] primarily due to the Fahraeus effect.[19] Finally, a decrease of tube diameter D results in a reduction of flow resistance, consistently with the Fahraeus–Lindqvist effect.[16,20]

The results discussed above can qualitatively be projected onto microvascular blood flow. In general, larger values of the ratio C between cytosol and plasma viscosities are expected to increase flow resistance in the microcirculation. Here, the effect of C is two-fold. First, the flow core formed by RBCs is frequently distorted at microvascular bifurcations and junctions, which is partially mimicked by the initially dispersed configuration of RBCs in our simulations. Our results suggest that RBC-FL convergence is obtained after a distance of $L_e \in (25D, 50D)$, which weakly increases with increasing C. The flow convergence distance should be compared with an average length of vessels (0.5–1 mm) within a branching network-like microvasculature,[1,4] e.g. L_e = 50D = 1 mm for D = 20 μm. This means that a converged flow within the microvasculature can only be expected in small vessels such as capillaries, while in microvessels with a diameter larger than about 10–20 μm, blood flow would likely always correspond to a transient (non-converged) flow. Therefore, differences in RBC-FL convergence for various C will contribute to the flow resistance in microvascular network. Second, the effect of C on flow resistance becomes more pronounced in vessels with diameters D > 20 μm. Such vessels represent a non-negligible part of the microvasculature, in which the resistance to blood flow is expected to increase with increasing C.

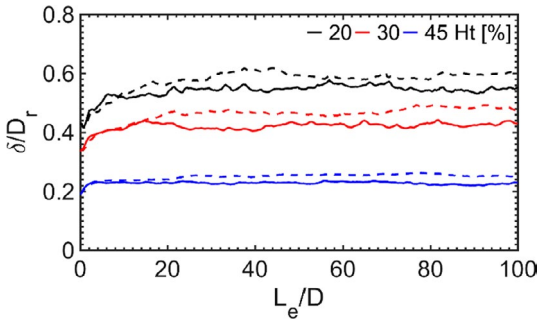

FIGURE 12 Development of the RBC-FL for $C = 1$ (solid lines) and $C = 5$ (dashed lines) suspensions and different hematocrits $H_t = 20\%$ (black), $H_t = 30\%$ (red), and $H_t = 45\%$ (blue). D = 20 μm and $Ca = 0.61$ ($\bar{\dot{\gamma}} = 377.4\,s^{-1}$)

Under normal physiological conditions, the average viscosity ratio of RBCs is estimated to be $C \approx 5$, which is primarily determined by the viscosity of the cytosol or the concentration of hemoglobin content. It is likely that a certain balance between the high hemoglobin content (implying large C) and low microvascular flow resistance exists to provide efficient oxygen delivery to tissues with acceptable work requirements for blood pumping by the heart. Our results and discussion above suggest that an increase in the blood flow resistance, when C is elevated from 1 to 5, is likely to be moderate, allowing a high hemoglobin content inside RBCs. Significant changes in C may occur in some pathologies such as sickle-cell anemia[45] and RBC hydration disorders.[46] For instance, RBCs from sickle-cell patients have the viscosity ratio up to $C = 30$,[45] which can significantly enhance the flow resistance and worsen oxygen delivery under already anemic conditions. However, drastic changes in microvascular blood flow, such as vessel blockages and ischemia, are unlikely to occur due to mere changes in RBC cytosolic viscosity, as they require significant elastic stiffening of RBCs and cell-wall adhesive interactions.[69]

TABLE 4 Relative viscosity η_{rel}, final RBC-FL thickness δ_f, and discharge hematocrit H_d for various tube diameters D. The tube hematocrit is fixed $H_t = 30\%$ and the flow is driven by a constant pressure gradient. The corresponding flow conditions and Ca are also shown in the table

D [μm]	40	20	15	10
$\bar{\dot{\gamma}}[s^{-1}]$	675	377	302	208
Ca	1.10	0.61	0.49	0.34
$\eta_{rel}^{C=1}$	1.39	1.27	1.25	1.12
$\eta_{rel}^{C=5}$	1.51	1.30	1.21	1.16
$\eta_{rel}^{C=5}/\eta_{rel}^{C=1} - 1$	8.5%	2.2%	−3.2%	3.2%
$\delta_f^{C=1}$ [μm]	3.19	2.77	2.18	1.21
$\delta_f^{C=5}$ [μm]	3.53	3.12	2.34	1.20
$H_d^{C=1}$	35.3%	33.2%	39.1%	38.0%
$H_d^{C=5}$	35.1%	33.3%	39.4%	37.5%

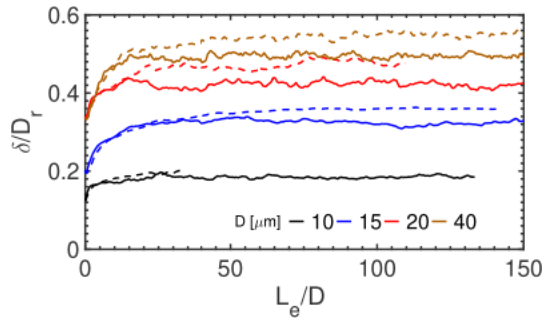

FIGURE 13 Development of the RBC-FL for $C = 1$ (solid lines) and $C = 5$ (dashed lines) suspensions and tube diameters D = 10 μm (black), D = 15 μm (blue), D = 20 μm (red), and D = 40 μm (brown). $H_t = 30\%$ with $\mathrm{Ca} > 0.34$ ($\bar{\dot{\gamma}} > 208\,\mathrm{s}^{-1}$) [Colour figure can be viewed at wileyonlinelibrary.com]

Finally, it is important to discuss the limitations of the presented model. Clearly, simulation results for blood flow in straight vessels cannot reflect the full complexity of blood flow in microvascular networks with diverse and dramatic changes in flow rates and patterns. There exist several recent simulation studies which model blood flow in small vessel networks, making an important step toward explicit microvascular flow modeling.[70] Furthermore, our simulations are performed in rigid tubes, while realistic microvascular vessels are flexible and can change their diameter in response to blood flow stresses[71] and biochemical signals.[72] Also, our model did not include aggregation interactions between RBCs, which result in the formation of rouleaux structures at low shear rates.[73] However, physiological aggregation interactions between RBCs are important only at low flow rates ($\bar{\dot{\gamma}} < 50\,\mathrm{s}^{-1}$) and would likely have no effect on our results, as we focused mainly on larger flow rates. A further prominent difference between blood flow in idealized rigid tubes and vessels in vivo is the presence of glycocalyx layer at the endothelial surface.[74] The glycocalyx is a brush-like flexible layer at the vessel walls, which may affect the flow rate and the interaction of RBCs with the wall.[75] These differences between microvascular flow in vivo and idealized blood flow in glass tubes significantly alter the Fahraeus–Lindqvist effect such that the flow resistance in small microvessels in vivo is estimated to be significantly larger than in the tubes of comparable diameter in vitro.[76,77] Further research is needed to dissect the importance of the discussed factors for microvascular blood flow.

5 | PERSPECTIVE

Our study shows that the dependence of blood flow resistance on the viscosity contrast $C \in [1, 20]$ in microvessels is rather moderate, even though the structure and dynamics of RBC suspension are different for various C values. These differences in flow behavior for different C are likely to be important for the margination of particles (e.g., platelets, drug-delivery carriers) in blood flow as well as for partitioning of RBCs within a complex microvascular network. In particular, the slow flow convergence behind branching points implies that many flow properties, such as resistance, particle margination, and oxygen delivery, can be highly inhomogeneous in complex vessel networks, depending on vessel diameters, branching lengths, and distance from the previous branching point. These aspects of blood flow need still to be addressed in future research.

ACKNOWLEDGEMENTS

The authors gratefully acknowledge the computing time granted through JARA-HPC on the supercomputer JURECA[78] at Forschungszentrum Jülich.

AUTHOR CONTRIBUTIONS

WC performed simulations and analyzed the data. GG and DAF designed the study. All authors discussed the results and wrote the manuscript.

ORCID

Wei Chien https://orcid.org/0000-0003-4162-4330
Gerhard Gompper https://orcid.org/0000-0002-8904-0986
Dmitry A. Fedosov https://orcid.org/0000-0001-7469-9844

REFERENCES

1. Popel AS, Johnson PC. Microcirculation and hemorheology. *Annu Rev Fluid Mech*. 2005;37:43-69.
2. Freund JB. Numerical simulation of flowing blood cells. *Annu Rev Fluid Mech*. 2014;46:67-95.
3. Fedosov DA, Noguchi H, Gompper G. Multiscale modeling of blood flow: from single cells to blood rheology. *Biomech Model Mechanobiol*. 2014;13:239-258.
4. Secomb TW. Blood flow in the microcirculation. *Annu Rev Fluid Mech*. 2017;49:443-461.
5. Zhao H, Shaqfeh ESG. Shear-induced platelet margination in a microchannel. *Phys Rev E*. 2011;83:061924.
6. Mehrabadi M, Ku DN, Aidun CK. Effects of shear rate, confinement, and particle parameters on margination in blood flow. *Phys Rev E*. 2016;93:023109.
7. Vahidkhah K, Diamond SL, Bagchi P. Platelet dynamics in three-dimensional simulation of whole blood. *Biophys J*. 2014;106:2529-2540.
8. Freund JB. Leukocyte margination in a model microvessel. *Phys Fluids*. 2007;19:023301.
9. Fedosov DA, Fornleitner J, Gompper G. Margination of white blood cells in microcapillary flow. *Phys Rev Lett*. 2012;108. https://doi.org/10.1103/PhysRevLett.108.028104
10. Fedosov DA, Gompper G. White blood cell margination in microcirculation. *Soft Matter*. 2014;10:2961-2970.
11. Fachin F, Spuhler P, Martel-Foley JM, et al. Monolithic chip for high-throughput blood cell depletion to sort rare circulating tumor cells. *Sci Rep*. 2017;7:10936.
12. Lin E, Cao T, Nagrath S, et al. Circulating tumor cells: diagnostic and therapeutic applications. *Annu Rev Biomed Eng*. 2018;20:329-352.
13. Lee T-R, Choi M, Kopacz AM, et al. On the near-wall accumulation of injectable particles in the microcirculation: smaller is not better. *Sci Rep*. 2013;3:2079.
14. Muller K, Fedosov DA, Gompper G. Margination of micro- and nano-particles in blood flow and its effect on drug delivery. *Sci Rep*. 2014;4:4871.
15. Cooley M, Sarode A, Hoore M, et al. Influence of particle size and shape on their margination and wall-adhesion: implications in drug delivery vehicle design across nano-to-micro scale. *Nanoscale*. 2018;10:15350-15364.

16. Pries AR, Secomb TW, Gaehtgens P, et al. Blood flow in microvascular networks. Experiments and simulation. *Circ Res*. 1990;67:826-834.
17. Skalak R, Keller SR, Secomb TW. Mechanics of blood flow. *J Biomech Eng*. 1981;103:102-115.
18. Lanotte L, Mauer J, Mendez S, et al. Red cells' dynamic morphologies govern blood shear thinning under microcirculatory flow conditions. *Proc Natl Acad Sci U S A*. 2016;113:13289-13294.
19. Fahraeus R. The suspension stability of the blood. *Physiol Rev*. 1929;9:241-274.
20. Fåhræus R, Lindqvist T. The viscosity of the blood in narrow capillary tubes. *Am J Physiol-Legacy Content*. 1931;96:562-568.
21. Pries AR, Neuhaus D, Gaehtgens P. Blood viscosity in tube flow: dependence on diameter and hematocrit. *Am J Physiol*. 1992;263:H1770-H1778.
22. Cokelet GR, Goldsmith HL. Decreased hydrodynamic resistance in the two-phase flow of blood through small vertical tubes at low flow rates. *Circ Res*. 1991;68:1-17.
23. Goldsmith HL, Cokelet GR, Gaehtgens P. Robin Fahraeus: evolution of his concepts in cardiovascular physiology. *Am J Physiol*. 1989;257:H1005-H1015.
24. Reinke W, Gaehtgens P, Johnson PC. Blood viscosity in small tubes: effect of shear rate, aggregation, and sedimentation. *Am J Physiol*. 1987;253:H540-H547.
25. Sharan M, Popel AS. A two-phase model for flow of blood in narrow tubes with increased effective viscosity near the wall. *Biorheology*. 2001;38:415-428.
26. Fedosov DA, Caswell B, Popel AS, et al. Blood flow and cell-free layer in microvessels. *Microcirculation*. 2010;17:615-628.
27. Lei H, Fedosov DA, Caswell B, et al. Blood flow in small tubes: quantifying the transition to the non-continuum regime. *J Fluid Mech*. 2013;722:214-239.
28. Katanov D, Gompper G, Fedosov DA. Microvascular blood flow resistance: Role of red blood cell migration and dispersion. *Microvasc Res*. 2015;99:57-66.
29. Geislinger TM, Franke T. Hydrodynamic lift of vesicles and red blood cells in flow—from Fahraeus & Lindqvist to microfluidic cell sorting. *Adv Colloid Interface Sci*. 2014. https://doi.org/10.1016/j.cis.2014.03.002
30. Pozrikidis C. Orbiting motion of a freely suspended spheroid near a plane wall. *J Fluid Mech*. 2005;541:105-114.
31. Olla P. The lift on a tank-treading ellipsoidal cell in a shear flow. *J Phys I*. 1997;7:1533-1540.
32. Grandchamp X, Coupier G, Srivastav A, et al. Lift and down-gradient shear-induced diffusion in red blood cell suspensions. *Phys Rev Lett*. 2013;110:108101.
33. Olla P. The role of tank-treading motions in the transverse migration of a spheroidal vesicle in a shear flow. *J Phys A-Math Gen*. 1997;30:317-329.
34. Abkarian M, Lartigue C, Viallat A. Tank treading and unbinding of deformable vesicles in shear flow: determination of the lift force. *Phys Rev Lett*. 2002;88:068103.
35. Messlinger S, Schmidt B, Noguchi H, et al. Dynamical regimes and hydrodynamic lift of viscous vesicles under shear. *Phys Rev E Stat Nonlin Soft Matter Phys*. 2009;80:011901.
36. Chen Y-L. Inertia- and deformation-driven migration of a soft particle in confined shear and Poiseuille flow. *RSC Adv*. 2014;4:17908.
37. Kumar A, Graham MD. Margination and segregation in confined flows of blood and other multicomponent suspensions. *Soft Matter*. 2012;8:10536.
38. Vollebregt HM, van der Sman RGM, Boom RM. Model for particle migration in bidisperse suspensions by use of effective temperature. *Faraday Discuss*. 2012;158:89-103.
39. Mauer J, Mendez S, Lanotte L, et al. Flow-induced transitions of red blood cell shapes under shear. *Phys Rev Lett*. 2018;121:118103.
40. Sinha K, Graham MD. Dynamics of a single red blood cell in simple shear flow. *Phys Rev E*. 2015;92:042710.
41. Yazdani A, Bagchi P. Influence of membrane viscosity on capsule dynamics in shear flow. *J Fluid Mech*. 2013;718:569-595.
42. Fischer TM. Shape memory of human red blood cells. *Biophys J*. 2004;86:3304-3313.
43. Skotheim JM, Secomb TW. Red blood cells and other nonspherical capsules in shear flow: oscillatory dynamics and the tank-treading-to-tumbling transition. *Phys Rev Lett*. 2007;98:078301.
44. Abkarian M, Faivre M, Viallat A. Swinging of red blood cells under shear flow. *Phys Rev Lett*. 2007;98:188302.
45. Byun H, Hillman TR, Higgins JM, et al. Optical measurement of biomechanical properties of individual erythrocytes from a sickle cell patient. *Acta Biomater*. 2012;8:4130-4138.
46. Caulier A, Rapetti-Mauss R, Guizouarn H, et al. Primary red cell hydration disorders: pathogenesis and diagnosis. *Int J Lab Hematol*. 2018;40(Suppl 1):68-73.
47. Wells R, Schmid-Schonbein H. Red cell deformation and fluidity of concentrated cell suspensions. *J Appl Physiol*. 1969;27:213-217.
48. Wells RE Jr, Merrill EW. Shear rate dependence of the viscosity of whole bllod and plasma. *Science*. 1961;133:763-764.
49. Freund JB, Orescanin MM. Cellular flow in a small blood vessel. *J Fluid Mech*. 2011;671:466-490.
50. Doddi SK, Bagchi P. Three-dimensional computational modeling of multiple deformable cells flowing in microvessels. *Phys Rev E Stat Nonlin Soft Matter Phys*. 2009;79:046318.
51. de Haan M, Zavodszky G, Azizi V, et al. Numerical investigation of the effects of red blood cell cytoplasmic viscosity contrasts on single cell and bulk transport behaviour. *Applied Sciences*. 2018;8:1616.
52. Saadat A, Guido CJ, Shaqfeh ESG. Effect of cytoplasmic viscosity on red blood cell migration in small arteriole-level confinements. *bioRxiv*. 2019. https://doi.org/10.1101/572933
53. Espanol P, Revenga M. Smoothed dissipative particle dynamics. *Phys Rev E*. 2003;67:026705.
54. Müller K, Fedosov DA, Gompper G. Smoothed dissipative particle dynamics with angular momentum conservation. *J Comp Phys*. 2015;281:301-315.
55. Noguchi H, Gompper G. Shape transitions of fluid vesicles and red blood cells in capillary flows. *Proc Natl Acad Sci U S A*. 2005;102:14159-14164.
56. Fedosov DA, Caswell B, Karniadakis GE. Systematic coarse-graining of spectrin-level red blood cell models. *Comput Methods Appl Mech Eng*. 2010;199:1937-1948.
57. Fedosov DA, Caswell B, Karniadakis GE. A multiscale red blood cell model with accurate mechanics, rheology, and dynamics. *Biophys J*. 2010;98:2215-2225.
58. Fedosov DA, Peltomaki M, Gompper G. Deformation and dynamics of red blood cells in flow through cylindrical microchannels. *Soft Matter*. 2014;10:4258-4267.
59. Español P, Warren P. Statistical mechanics of dissipative particle dynamics. *Europhys Lett*. 1995;30:191-196.
60. Hoogerbrugge PJ, Koelman JMVA. Simulating microscopic hydrodynamic phenomena with dissipative particle dynamics. *Europhys Lett*. 1992;19:155-160.
61. Fedosov DA, Karniadakis GE. Triple-decker: Interfacing atomistic-mesoscopic-continuum flow regimes. *J Comp Phys*. 2009;228:1157-1171.
62. Suresh S, Spatz J, Mills JP, et al. Connections between single-cell biomechanics and human disease states: gastrointestinal cancer and malaria. *Acta Biomater*. 2005;1:15-30.
63. Fedosov DA, Caswell B, Suresh S, et al. Quantifying the biophysical characteristics of Plasmodium-falciparum-parasitized red blood cells in microcirculation. *Proc Natl Acad Sci U S A*. 2011;108:35-39.
64. Kim S, Kong RL, Popel AS, et al. Temporal and spatial variations of cell-free layer width in arterioles. *Am J Physiol Heart Circ Physiol*. 2007;293:H1526-H1535.

65. Narsimhan V, Zhao H, Shaqfeh ESG. Coarse-grained theory to predict the concentration distribution of red blood cells in wall-bounded Couette flow at zero Reynolds number. *Phys Fluids*. 2013;25:061901.
66. Abkarian M, Viallat A. Dynamics of vesicles in a wall-bounded shear flow. *Biophys J*. 2005;89:1055-1066.
67. McWhirter JL, Noguchi H, Gompper G. Flow-induced clustering and alignment of vesicles and red blood cells in microcapillaries. *Proc Natl Acad Sci U S A*. 2009;106:6039-6043.
68. Pries AR, Secomb TW, Gaehtgens P. Structure and hemodynamics of microvascular networks: heterogeneity and correlations. *Am J Physiol*. 1995;269:H1713-H1722.
69. Fedosov DA. In silico modeling of malaria and sickle-cell disease. *Drug Discov Today: Dis Models*. 2015;16:17-22.
70. Balogh P, Bagchi P. Three-dimensional distribution of wall shear stress and its gradient in red cell-resolved computational modeling of blood flow in in vivo-like microvascular networks. *Physiol Rep*. 2019;7:e14067.
71. Lighthill MJ. Pressure-forcing of tightly fitting pellets along fluid-filled elastic tubes. *J Fluid Mech*. 2006;34:113-143.
72. Reglin B, Secomb TW, Pries AR. Structural adaptation of microvessel diameters in response to metabolic stimuli: where are the oxygen sensors? *Am J Physiol Heart Circ Physiol*. 2009;297:H2206-H2219.
73. Cokelet G, Merrill EW, Gilliland ER, et al. The rheology of human blood-measurement near and at zero shear rate. *Trans Soc Rheol*. 1963;7:303-317.
74. Weinbaum S, Tarbell JM, Damiano ER. The structure and function of the endothelial glycocalyx layer. *Annu Rev Biomed Eng*. 2007;9:121-167.
75. Damiano ER. The effect of the endothelial-cell glycocalyx on the motion of red blood cells through capillaries. *Microvasc Res*. 1998;55:77-91.
76. Pries AR, Secomb TW, Gessner T, et al. Resistance to blood flow in microvessels in vivo. *Circ Res*. 1994;75:904-915.
77. Secomb TW, Pries AR. Blood viscosity in microvessels: Experiment and theory. *C R Phys*. 2013;14:470-478.
78. Krause D, Thörnig P. JURECA: modular supercomputer at Jülich Supercomputing Centre. *JLSRF*. 2018;4:132.

How to cite this article: Chien W, Gompper G, Fedosov DA. Effect of cytosol viscosity on the flow behavior of red blood cell suspensions in microvessels. *Microcirculation*. 2021;28:e12668. https://doi.org/10.1111/micc.12668